Scanning Microwave Microscopy of Polarization Domain Boundaries in 2D SnSe

Yawei Zhang[1], Xiaopeng Wang[1], Marco Farina[1], James C. M. Hwang[1], Yunyue Zhu[2], Nannan Mao[2], Peng Wu[2], Jing Kong[2]

[1]Cornell University, Ithaca, NY, USA, [2]Massachusetts Institute of Technology, Cambridge, MA, USA

***Abstract* — Scanning microwave microscopy (SMM) allows for nanoscale characterization of in-plane polarization domains in 2D atomic-layered SnSe. Previous SMM studies found significantly higher conductivity at domain boundaries than in the domain interior. Here, we successfully use SMM to distinguish 90° and 180° domain boundaries not revealed by polarized optical microscopy or atomic force microscopy. Quantitative analysis results in significantly higher conductivity in 180° domain boundaries than in 90° domain boundaries and, in turn, inside domains. We attribute the enhanced conductivity to polarization-induced two-dimensional electron or hole gas similar to that in GaN high-electron mobility transistors. This work demonstrates SMM's efficacy for non-destructive, in situ monitoring of 2D materials and devices.**

***Index Terms* — Atomic force microscopy, two-dimensional electron gas (2DEG), two-dimensional material, polarization domain, scanning microwave microscopy**

I. Introduction

2D atomic-layered SnSe has garnered significant attention in nanoelectronics and optoelectronics due to its exceptional properties, including in-plane ferroelectricity, high thermoelectric coefficients, and nonlinear optical characteristics [1]. Recent advancements in low-pressure physical vapor deposition have enabled the synthesis of high-quality 2D SnSe layers with controlled thicknesses [1]. However, it has been challenging to use conventional material characterization techniques such as optical microscopy and atomic force microscopy (AFM) to determine the structural or electrical properties of 2D SnSe at the nanoscale.

In comparison, scanning microwave microscopy (SMM) has emerged as a versatile tool for both structural and electrical characterization of semiconductors, dielectrics, and biological cells [2]–[11]. Recently, we have used SMM to reveal in-plane domain boundaries in 2D SnSe [12]. This paper further quantifies the conductivity of 90° and 180° domain boundaries.

II. Method

A. *SnSe Samples*

2D SnSe flakes are synthesized using low-pressure physical vapor deposition [1]. The synthesis begins by placing SnSe powder precursor in a crucible at the center of a tube furnace. A freshly exfoliated mica substrate, annealed at 400 °C in air for 10 min, is positioned 10-cm downstream from the precursor. The furnace is then evacuated to 10 mTorr and heated to 420 °C for a deposition of approximately 40 min. After deposition, the furnace is quickly cooled to room temperature [1]. Finally, SnSe flakes are transferred using polymethyl methacrylate (PMMA) from mica to a doped Si substrate precoated with 300-nm-thick SiO_2. The synthesized SnSe flakes are up to 23-μm wide with a thickness of 2 to 15 nm. Using a Zeiss reflected light microscope, Fig. 1 shows a linearly polarized optical micrograph of the flakes on the Si substrate. Note that the region between the flakes where the Si substrate is exposed can be used for SMM calibration as described in Sec. II.B.

With linearly polarized transverse electromagnetic waves, optical microscopy can distinguish between domains with orthogonal (90° difference) polarizations, but not between domains with opposite (180° difference) polarizations (Fig. 2). Similarly, with transverse magnetic waves, SMM cannot distinguish between domains with opposite polarizations. However, unlike optical microscopy, SMM has sufficient spatial resolution to resolve domain boundaries, especially when they are more conductive than the domain interior [12].

Specifically, when the in-plane polarization of a ferroelectric domain is parallel to the polarization of the incident light, optical absorption is maximized while reflection is minimized, resulting in the darkest contrast. Conversely, for domains with polarization perpendicular to that of the incident light, optical coupling is minimized, resulting in the highest reflection and the brightest contrast in the micrograph. Although optical microscopy does not have sufficient spatial resolution to resolve domain boundaries, for 90° domain boundaries [Fig. 2(a)], contrast exists between neighboring domains of orthogonal polarizations, making the boundary between bright and dim regions visible. However, for 180° domain boundaries [Fig. 2(b)], there is no contrast between domains of opposite polarizations, so the boundary between the two domains is not visible under the optical microscope.

B. *SMM Setup and Analysis*

Fig. 3. illustrates the SMM/AFM setup. It is based on a Keysight Technologies 7500 AFM equipped with an N9545C SMM nose cone [11]. A Rocky Mountain 25Pt300A platinum probe, featuring a spring constant of 18 N/m and a tip radius of 25 nm, serves as the dual-function AFM/SMM probe. This probe is affixed to a platinum cantilever 300-μm long, 60-μm wide, and 2-μm thick. The cantilever is connected to a Keysight Technologies E8062B vector network analyzer (VNA) via coaxial cables. For impedance matching around 3 GHz and its harmonics, the cables are shunted with a 50 Ω resistor. The

979-8-3315-9080-2/26/$31.00 ©2026 IEEE

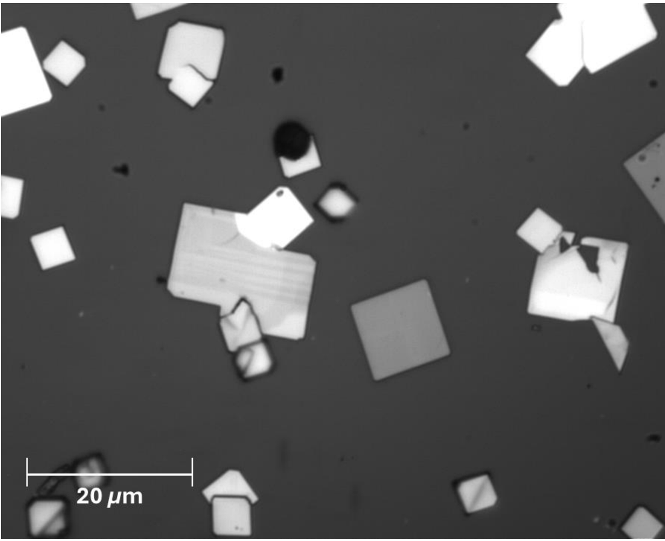

Fig. 1. Linearly polarized optical micrograph of SnSe flakes on the Si substrate. Dark circles are PMMA residues.

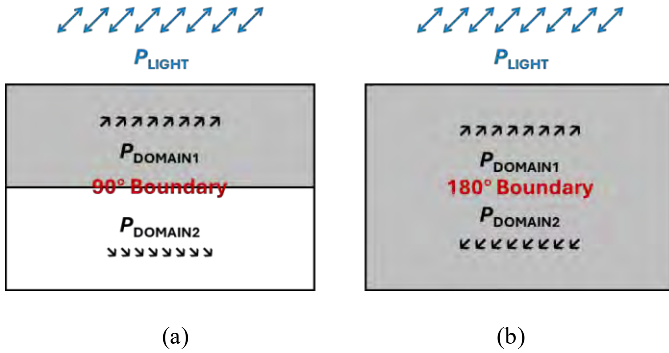

Fig. 2. Schematics illustration of the mechanism in polarized optical microscopy of in-plane polarized domains, showing (a) contrast between domains with orthogonal polarizations and (b) lack of contrast between domains with opposite polarizations. In either case, optical microscopy does not have sufficient spatial resolution to resolve domain boundaries.

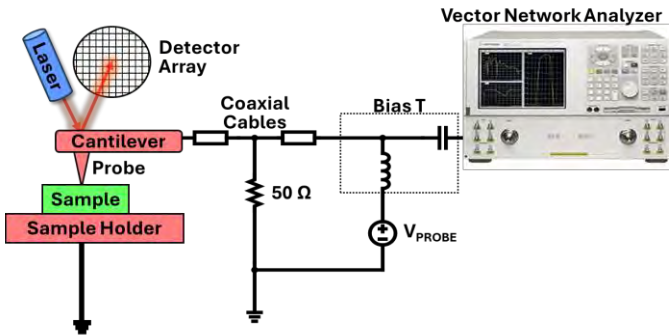

Fig. 3. Schematics of the AFM-based SMM.

VNA generates a 0-dBm signal at 15.7 GHz, which incidents from the probe to the sample. This power level is selected to provide an adequate signal-to-noise ratio (SNR) while minimizing sample destruction. The 15.7-GHz frequency is chosen to maximize image contrast because the higher the frequency, the higher the sensitivity to small capacitances [7]. Frequencies higher than 15.7 GHz cannot be used because the setup has a bandwidth of 18 GHz. The VNA detects the signal reflected from the sample following its near-field interaction with the probe and records the reflection coefficient S_{11}. The intermediate frequency bandwidth of the VNA is set to 500 Hz, balancing SNR and scan rate. Under these conditions, a 15 μm × 15 μm area can be scanned at a resolution of 256 × 256 pixels in approximately 4 min, corresponding to a scan rate of 200 pixels/s. During the same scan, SMM and AFM signals are simultaneously detected and recorded.

C. *SMM Data* Analysis

The measured S_{11} is converted to the probe-sample interaction admittance Y by one-port *in situ* calibration [2], [3]. The calibration is based on measuring S_{11} as the probe approaches the bare substrate between the SnSe flakes, while measuring the probe-sample capacitance C using the AFM in the mode of electrostatic force microscopy. By acquiring both S_{11}(z) and C(z) as functions of the probe-sample distance z, the error-correction coefficients e_{00}, e_{01}, and e_{11} are extracted for converting S_{11} to Y. Additionally, the probe geometry, such as the tip radius and the cone angle/height of the probe body are extracted by fitting C(z) curves with simulated probe characteristics [3]. This *in situ* calibration enables quantitative and non-destructive mapping of the local capacitance and conductance of the 2D SnSe flakes with resolution comparable to the tip radius.

After S_{11} is converted to Y, it is used to extract the conductivity of SnSe flakes using a simple equivalent circuit model validated by numerical simulations [11]. To this end, three-dimensional finite-element electromagnetic simulations are performed using the COMSOL AC/DC module. The equivalent circuit model, tailored to the present sample structure, consists of three elements: C_1, representing all dielectric layers above the conducting substrate with their respective dielectric constants and thicknesses; C_2, accounting for the fringing capacitance between the sample and the probe body; and

$$G_0 = 1/R_{SHEET} = t/\rho, \tag{1}$$

where R_{SHEET} is the sheet resistance, t is the thickness, and ρ is the resistivity of a SnSe flake.

Therefore,

$$Y = G + j\omega C = j\omega C_2 + j\omega G_0 C_1/(G_0 + j\omega C_1), \tag{2}$$

where ω is the angular frequency of the incident signal. Note that $Y \approx j\omega C_2$ when the SMM is scanning over the bare substrate not covered by any SnSe flake.

The admittance contrast between a SnSe flake and a bare substrate area is

$$\Delta Y = j\omega G_0 C_1/(G_0 + j\omega C_1). \tag{3}$$

The conductance contrast ΔG and capacitance contrast ΔC are

$$\Delta G = G_0 \omega^2 C_1^2 / (G_0^2 + \omega^2 C_1^2), \quad (4)$$

and

$$\Delta C = G_0^2 C_1 / (G_0^2 + \omega^2 C_1^2). \quad (5)$$

Using this model, we solve the inverse problem by first simulating ΔG and ΔC for various G_0 values. Then, by fitting the simulated ΔG and ΔC to their measured values, we determine the G_0 value that best matches. Using (1) with G_0 extracted by SMM and t determined by AFM, we calculate ρ.

III. Results and Discussion

SnSe flakes are characterized by simultaneous SMM/AFM. Fig. 4(a) shows that AFM cannot resolve polarization domains at all. By contrast, Fig. 4(b) shows dark striations in the SMM resistivity image corresponding to polarization domain boundaries. The darker the striation, the higher the conductivity. This implies that the domain boundaries are more conductive than the domain interiors are, as evident in the SMM line scan along the dashed line, crossing four striations. By analyzing SnSe flakes of various thicknesses (2–6 nm), it shows $\rho \approx 0.02$ Ω·m in the domain interior, whereas $\rho \approx 0.007$ Ω·m at the domain boundary. These values are in general agreement with current-voltage (I-V) characteristics measured on devices fabricated on thin (≤ 6 nm) SnSe flakes with Ti/Pt electrodes, resulting in an average resistivity of approximately 0.004 Ω·m. Note that although average resistivity is calculated from the overall current-voltage characteristics across both domain interiors and domain boundaries, conduction tends to be dominated by domain boundaries due to their much higher conductivity.

With rotational symmetry, the transverse magnetic waves of SMM interact equally with domains with in-plane polarizations of all directions. However, SMM has sufficient spatial resolution to reveal domain boundaries as dark striations that coincide with 90° domain boundaries between bright and dark regions in optical microscopy, and the darkest striations where optical microscopy shows no contrast. In other words, SMM reveals additional details of regions appearing uniformly bright in optical micrographs, indicating the presence of 180° domain boundaries. Fig. 5 illustrates the detection by SMM of both 90° and 180 domain boundaries in three flakes with (a) equally distributed 90° and 180° domain boundaries, (b) only 90° domain boundaries, and (c) predominantly 180° domain boundaries.

IV. Conclusion

In this study, we use SMM to characterize the resistivity of 2D SnSe flakes. We demonstrate the unique capability of SMM in non-destructive resistivity mapping at the nanoscale. This is

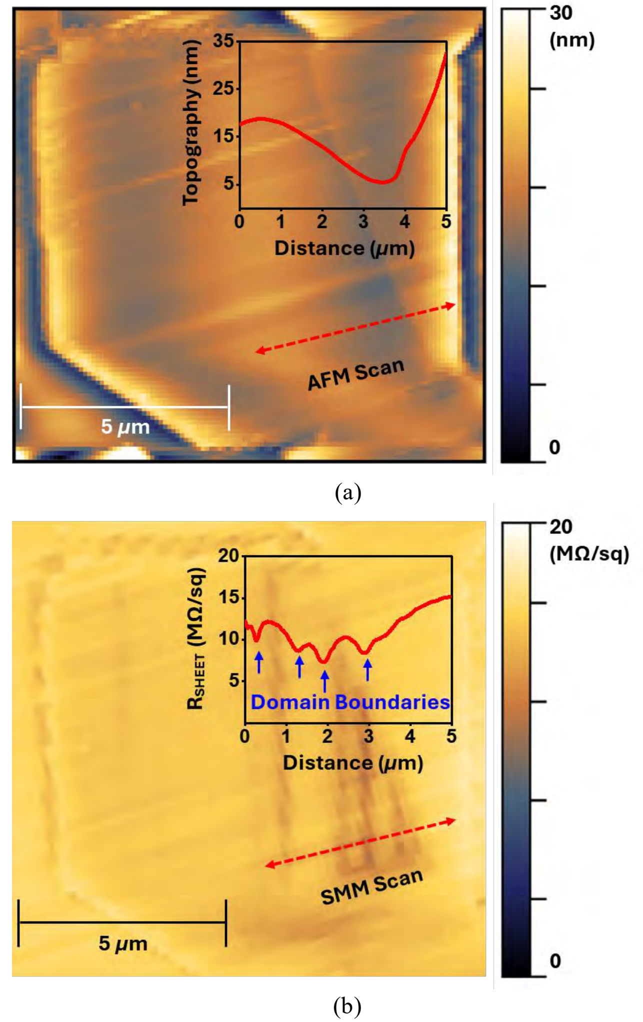

Fig. 4. (a) AFM micrograph with a linear scan along the dashed trace showing lack of topography featured. (b) SMM resistivity image of the same flake with a linear scan along the same dashed trace showing resistivity dips indicating domain boundaries.

a distinctive advantage over conventional contactless resistivity mapping methods such as the four-point probe [13], Van der Pauw [14], eddy current [15], and Hall effect [16], which are capable of only millimeter-scale resolution and are applicable only to raw materials instead of device structures. Using SMM, we have previously imaged laterally distributed 2D electron gas and 2D hole gas in GaN high electron mobility transistors. We now use SMM to image vertically distributed 2D electron or hole gas in SnSe. It helps advance the understanding of quantum-confined transport in ferroelectric 2D materials bridging theoretical predictions with experimental observations. This work establishes a comprehensive framework correlating polarization domains with device performance, bridging theoretical predictions with experimental observations.

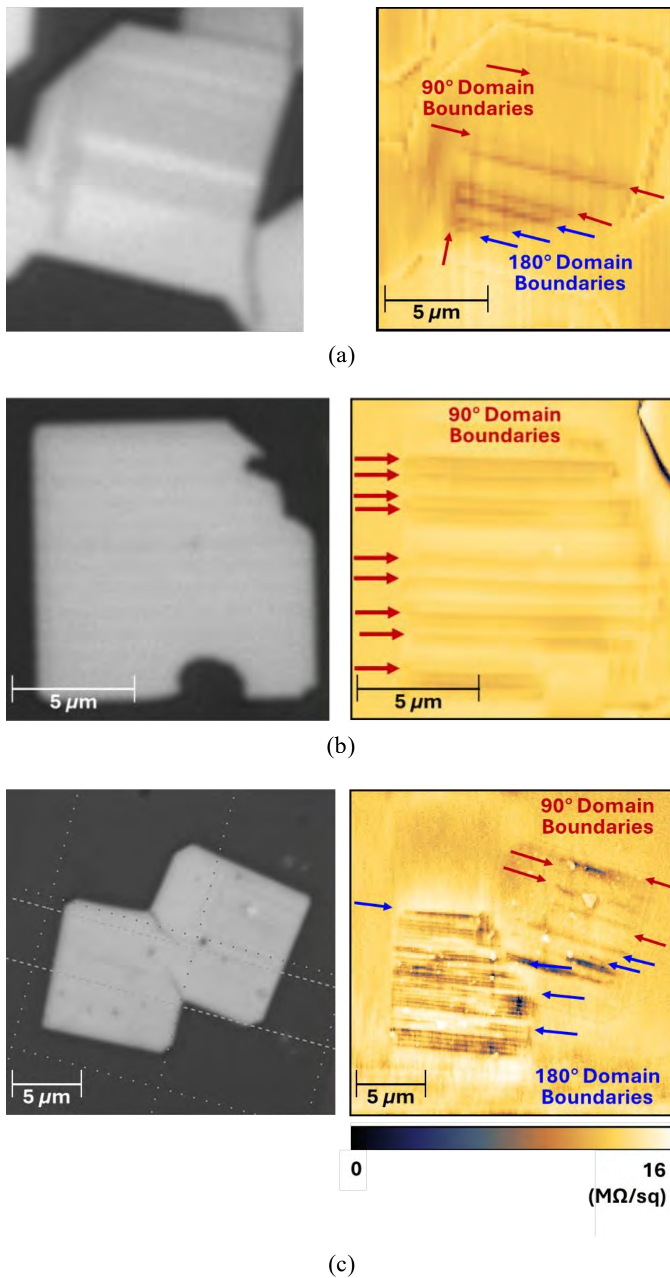

Fig. 5. Polarized optical micrographs (left) and SMM resistivity images (right) of three SnSe flakes with (a) equally distributed 90° and 180° domain boundaries, (b) only 90° domain boundaries, and (c) predominantly 180° domain boundaries.

Acknowledgement

This work was supported in part by in part by SUPREME, one of the seven centers sponsored by the Semiconductor Research Corporation and the U.S. Defense Advanced Projects Agency through the Joint University Microelectronics Program 2.0 under Contract 2023-JU-3137 This work was performed in part at the Cornell NanoScale Facility, an NNCI member supported by NSF Grant NNCI-2025233.

References

[1] M.-H. Chiu *et al.,* "Growth of large-sized 2D ultrathin SnSe crystals with in-plane ferroelectricity," *Adv. Electron. Mater.*, vol. 9, no. 4, p. 2201031, Apr. 2023.

[2] M. Farina, D. Mencarelli, A. Di Donato, G. Venanzoni and A. Morini, "Calibration protocol for broadband near-field microwave microscopy," *IEEE Trans. Microw. Theory Techn.,* vol. 59, no. 10, pp. 2769–2776, Oct. 2011.

[3] G. Gramse, M. Kasper, L. Fumagalli, G. Gomila, P. Hinterdorfer, and F. Kienberger, "Calibrated complex impedance and permittivity measurements with scanning microwave microscopy," *Nanotechnol.*, vol. 25, no. 14, p. 145703, Mar. 2014.

[4] M. Farina *at al.,* "Inverted scanning microwave microscope for in vitro imaging and characterization of biological cells," *Appl. Phys. Lett*., vol. 114, no. 9, p. 093703, Mar. 2019.

[5] R. C. Chintala, K. Rubin, and Y. Yang, "Scanning microwave impedance microscopy: Room-temperature and low-temperature applications for device and material characterization," *IEEE Microw. Mag.*, vol. 21, no. 10, pp. 22–35, Oct. 2020.

[6] S. Berweger, T. M. Wallis, and P. Kabos, "Nanoelectronic characterization: Using near-field microwave microscopy for nanotechnological research," *IEEE Microw. Mag.*, vol. 21, no. 10, pp. 36–51, Oct. 2020.

[7] M. Farina and J. C. M. Hwang, "Scanning microwave microscopy for biological applications: Introducing the state of the art and inverted SMM," *IEEE Microw. Mag.*, vol. 21, no. 10, pp. 52–59, Oct. 2020.

[8] L. Zheng, L. Shao, M. Loncar, and K. Lai, "Imaging acoustic waves by microwave microscopy: Microwave impedance microscopy for visualizing gigahertz acoustic waves," *IEEE Microw. Mag.*, vol. 21, no. 10, pp. 60–71, Oct. 2020.

[9] A. Tselev, "Near-field microwave microscopy: Subsurface imaging for in situ characterization," *IEEE Microw. Mag.*, vol. 21, no. 10, pp. 72–86, Oct. 2020.

[10] X. Wang *et al.,* "Inverted scanning microwave microscopy of GaN/AlN high-electron mobility transistors," in *2024 103rd ARFTG Microw. Meas. Conf. (ARFTG),* Washington, DC, USA, Jun. 2024, pp. 1–4.

[11] X. Wang *et al.*, "Quantitative Scanning microwave microscopy for transfer characteristics of GaN high-electron-mobility transistors," *IEEE Trans. Microw. Theory Techn.*, vol. 73, no. 3, pp. 1573–1580, Mar. 2025.

[12] Y. Zhang, X. Wang, J. C. M. Hwang, N. Mao, P. Wu, and J. Kong, "Characterization of in-plane polarization domains in 2D SnSe by scanning microwave microscopy," in *2025 104th ARFTG Microw. Meas. Symp. (ARFTG),* San Juan, PR, USA, Jan. 2025, pp. 1–4.

[13] I. Miccoli, F. Edler, H. Pfnür, and C. Tegenkamp, "The 100th anniversary of the four-point probe technique: the role of probe geometries in isotropic and anisotropic systems," *J. Physics: Condens. Matter*, vol. 27, no. 22, p. 223201, May 2015.

[14] X. Hu, L. Zhu, K. Diao, W. Liu, X. Deng, and H. Wang, "Electrostatic derivation for the van der Pauw formula and simulation using arbitrarily shaped resistive materials," *AIP Adv.*, vol. 12, no. 7, p. 075208, Jul. 2022.

[15] X J. E. Neighbor, "Eddy-current method for measuring anisotropic resistivity," *J. Appl. Phys.*, vol. 40, no. 8, pp. 3078–3080, Jul. 1969.

[16] F. Werner, "Hall measurements on low-mobility thin films," *J. Appl. Phys.*, vol. 122, no. 13, p. 135306, Oct. 2017.